The Journal of the Acoustical Society of America

OCTOBER 19 2026

Source centering of directivity patterns using acoustical holography and magnitude far-field pattern equivalence

Samuel D. Bellows ; Timothy W. Leishman

Check for updates

J. Acoust. Soc. Am. 160, 3161–3172 (2026)
https://doi.org/10.1121/10.0046846

View Online Export Citation

Articles You May Be Interested In

Near-field acoustic holography with iteratively reweighted least squares–based outlier rejection and TV+ℓ_1 regularization

J. Acoust. Soc. Am. (September 2026)

Complete de-Dopplerization and acoustic holography for external noise of a high-speed train

J. Acoust. Soc. Am. (September 2016)

Subresolution in microwave holography

AIP Conf. Proc. (December 1980)

21 October 2026 17:59:12

ASA LEARN MORE
Advance your science and career as a member of the
Acoustical Society of America

ASA ACOUSTICAL SOCIETY OF AMERICA

JASA ARTICLE

Source centering of directivity patterns using acoustical holography and magnitude far-field pattern equivalence

Samuel D. Bellows[1,2,a] and Timothy W. Leishman[1]
[1]Acoustics Research Group, Department of Physics and Astronomy, Brigham Young University, Provo, Utah 84602, USA
[2]University of Utah Asia Campus, 119-3 Songdo Moonhwa-Ro, Yeonsu-Gu Incheon 21985, Republic of Korea

ABSTRACT:
Two essential points of consideration for spherical directivity measurements are the measurement radius and the sound source's location relative to the evaluation surface. When spatial constraints, such as anechoic chamber size, limit the measurement radius, both points may lead to measured near-field directivity patterns deviating from the desired far-field radiation characteristics. To clarify the impact of source placement on near-field and far-field radiation patterns, this work develops far-field magnitude and phase relations between untranslated and translated sources. The resulting theory shows that far-field propagation *via* acoustical holography is sufficient to correct for source-positioning uncertainties, provided that the measurements incorporate sufficient sampling positions to avoid spatial aliasing. The magnitude equivalence of translated and untranslated far-field directivity patterns also enables an acoustic centering procedure that overcomes previous low-frequency limitations.
© 2026 Acoustical Society of America. https://doi.org/10.1121/10.0046846
(Received 10 April 2026; revised 16 September 2026; accepted 17 September 2026; published online 19 October 2026)
[Editor: Mingsian R. Bai] Pages: 3161–3172

I. INTRODUCTION

Directivities are crucial characteristics of sound sources with applications to auralization,[1] room acoustical design,[2,3] microphone placement,[4,5] and other areas of acoustics. With the growing availability and usage of directivity data for many sound sources, researchers and practitioners would benefit from an increased understanding of associated concepts and improved tools for directivity measurements, post-processing, and implementation. This paper addresses this need in two specific areas: radial directivity dependence and acoustic centering *via* acoustical holography.

A directivity function characterizes a source's spatio-spectral radiation amplitude dependence and has standardized definitions such as "the … level … as a function of the direction of propagation of the radiated … sound … at a specified frequency."[6] Beranek and Mellow[7] judiciously noted that it also depends upon the observation distance, with radial dependence vanishing only in the source's acoustic and geometric far field. Even though some of the earliest directivity measurements considered radial directivity dependencies,[8,9] most researchers and practitioners today employ directional data measured or modeled at constant radii of arbitrary distance as though they were radially independent far-field values, whether that assumption is technically valid or not.

The radial dependence of sound radiation implies that source alignment during directivity measurements is significant, particularly when constraints, such as anechoic chamber size, restrict measurements to the source's near field. To cause near-field directivity results to represent the desired far-field pattern, Ureda[10] sought to place a loudspeaker at its so-called apparent apex or acoustic center. He made several salient observations throughout his works on the topic: (1) placing a source at the acoustic center does not guarantee representative far-field results, (2) directivity balloons change with measurement radius until converging to the far-field pattern, (3) the acoustic center shifts over frequency, and (4) distance is more important than point of rotation for directivity measurements.[10–12]

Other researchers developed different ideas about acoustic centers, with applications outside directivity measurements such as transducer calibration,[13,14] sound attenuation,[15] and evaluating the anechoic properties of rooms.[16,17] Trott[18] argued that the acoustic center should be defined as the location of an equivalent point source that produces the same complex-valued far-field pressure. Most standardized definitions of the acoustic center, such as "the position of the virtual point source from which sound pressure varies inversely as distance"[6] or "the point from which … spherical wavefronts … appear to diverge"[19] follow from Trott's[18] redefinition. However, Jacobsen *et al.*[20] demonstrated that replacing an extended source by an equivalent point source is an inconsistent definition because different approaches, such as matching $1/r$ decays or phase shifts, do not give the same acoustic center, even for the *same* theoretical source.

Instead of using the approaches reviewed by Jacobsen *et al.*,[20] Vanderkooy and Henwood[21,22] established the location of an equivalent point source by exploiting the point about which one takes a multipole expansion of the Kirchhoff–Helmholtz integral theorem (KHIT) to remove the dipole moment. Assuming the higher-order (e.g., quadrupole) terms are negligible, only the monopole moment remains. Vanderkooy and Henwood's[21,22] numerical and experimental results confirmed the empirical results shown by Ureda,[10–12] such as significant improvements in predicting the expected

[a]Email: samuel.bellows11@gmail.com

21 October 2026 17:59:12

far-field behaviors from near-field measurements. However, this low-frequency acoustic center is only valid for omnidirectional radiators when the acoustic wavelength is larger than the source's dimensions,[21–23] although some analytical expressions may be derived for dipole sources.[24]

Other approaches have attempted to generalize the essence of Vanderkooy and Henwood's[21,22] work to higher frequencies through spherical harmonic expansions as part of the Helmholtz equation exterior solution, which converges at all frequencies. Because the low-degree terms of the expansion correspond to multipole moments,[23,25] Deboy[28] localized the acoustic center by numerically optimizing the expansion origin to minimize the contribution of higher-degree terms. Ben Hagai *et al.*[26] studied the same objective function proposed by Deboy,[28] plus four other optimization criteria to define the acoustic center. One criterion involved maximizing the power of the zero-degree (monpole) term, analogous to Vanderkooy's[22] approach. Rather than directly penalizing higher-degree terms, Hargreaves[27] explored centering of a cardioid loudspeaker based on the spherical harmonic expansion's convergence rate.

These expansion-based energy-minimization approaches yielded reasonable results at lower frequencies, but spatial aliasing effects limited their application. Deboy[28] found well-defined minima up to around 1 kHz using a 64-point measurement scheme, whereas the 32-point array employed in Ben Hagai *et al.*[26] only allowed consistent results up to around 400 Hz. The latter result is consistent with findings in Ref. 29, which demonstrated that spatial aliasing occurs for this 32-point sampling scheme around 500 Hz when used for musical instrument directivity measurements.

In addition to expansion-based techniques, another acoustic centering approach involved minimizing the tangential components of the acoustic intensity.[30] Other methods have attempted, through various means, to exploit phase differences to localize the acoustic center.[28,31,32]

Although these past techniques are plausible for source centering at low and intermediate frequencies, they lack robustness when their underlying assumptions fail. For example, equivalent monopole techniques are only valid at low frequencies when the source directivity is omnidirectional.[22,23] Low-degree energy assumptions likewise cannot be valid at arbitrary frequencies because complex radiation patterns require higher-degree terms at higher frequencies.[29] Additionally, although phase-based approaches may converge at higher frequencies, they generally require spatial phase uniformity or symmetry, which limits their generalization.[32]

To overcome these disadvantages, this work first derives the relationship between the directivity patterns of a translated and untranslated source. The result shows that the far-field magnitude patterns of both centered and translated directivities are equivalent. Consequently, numerical far-field propagation can replace source-centering algorithms for many practical applications requiring the far-field magnitude pattern. This work then presents a source-centering method based on far-field directivity patterns, expanding upon preliminary results previously reported by Bellows and Leishman.[33] Because all sources have fixed-magnitude far-field patterns at any specified frequency, the technique overcomes previous low-frequency assumptions. Theoretical models and experimental results on a measured loudspeaker provide methodological validations, although adequate sampling is critical to minimize spatial aliasing.

II. THEORY

A. Far-field nature of radiating sources

Consider a source with a defining boundary S radiating into an acoustic domain Ω as depicted in Fig. 1(a). If a spherical surface of radius $r = a$ entirely encloses the boundary, the unique solution of the complex-valued pressure p to the Helmholtz equation for the spherical exterior domain, indicated here as $\Omega_a \subset \Omega$, is[25]

$$p(r,\theta,\phi,k) = \sum_{n=0}^{\infty}\sum_{m=-n}^{n} c_n^m(k) h_n^{(2)}(kr) Y_n^m(\theta,\phi), \quad r \geq a, \tag{1}$$

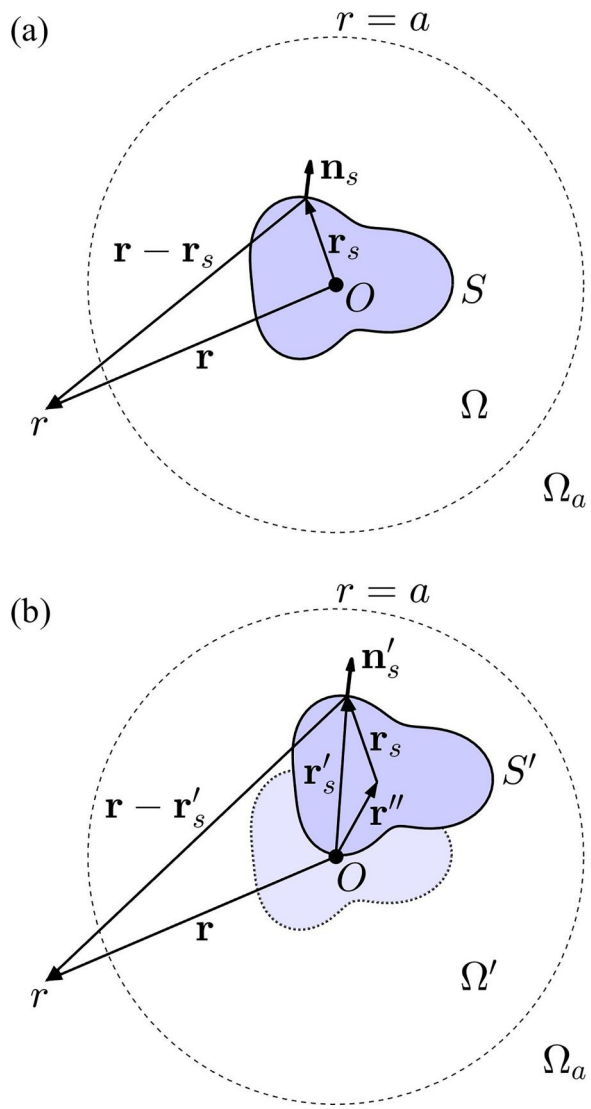


FIG. 1. A depiction of an acoustic source contained within a spherical surface of radius $r = a$ (a) before and (b) after translation by $\mathbf{r}''$.

21 October 2026 17:59:12

https://doi.org/10.1121/10.0046846

where k is the acoustic wavenumber, $c_n^m(k)$ are the frequency-dependent expansion coefficients, $h_n^{(2)}$ are the spherical Hankel functions of the second kind of order n (for outward-going waves with $e^{i\omega t}$ time dependence), and Y_n^m are the normalized spherical harmonics of degree n and order m. The pressure expansion coefficients c_n^m follow by exploiting the orthogonality of the spherical harmonics on the $r = a$ boundary, such that

$$c_n^m(k) = \frac{1}{h_n^{(2)}(ka)} \int_0^{2\pi} \int_0^{\pi} p(a,\theta,\phi,k) Y_n^{m*}(\theta,\phi) \sin\theta d\theta d\phi, \tag{2}$$

where * denotes complex conjugation. Practically, the expansion coefficients may result from numerical integration or a least squares approach.[34]

It is critical to note that there is no requirement placed on the location of the source provided that the spherical surface fully encloses it. Equation (1) consequently remains valid even if the coordinate system origin and the acoustic source center (if it exists) are not aligned. The pressure expansion coefficients c_n^m provide both the unique solution on Ω_a and other field variables, including the particle velocity, time-averaged intensity, and time-averaged sound power. This extrapolation of field variables for $r > a$ corresponds to acoustical holography.[25] Near-field acoustical holography and other inverse methods allow extrapolation of field variables for $r < a$, although these techniques are limited because of their inherent nonuniqueness.[25]

Many practical source directivity applications require only the far-field pressure, where r satisfies $kr \gg 1$ or $r \gg \lambda/2\pi$ (the acoustic far field) and $r \gg R_s$ (the geometric far field), where R_s represents the source's maximum spatial extent from the origin.[35] In the acoustic far field, the large-argument spherical Hankel function approximation allows separation of the radial and angular portions of the solution in Eq. (1), such that

$$p(r,\theta,\phi,k) \approx \frac{e^{-ikr}}{r} \sum_{n=0}^{\infty} \sum_{m=-n}^{n} c_n^m(k) k^{-1} i^{n+1} Y_n^m(\theta,\phi). \tag{3}$$

Similar to a simple source, the wave takes on spherical spreading, such that the sound pressure varies inversely with distance, a common basis for determining the acoustic center. However, unlike a spherical wave produced by a simple source, the complex pressure has an angular dependence that is independent of the radial observation distance r. Additionally, although a simple source has constant phase across the spherical surface or wavefront,[6] for an arbitrary source there is no restriction on its phase. An unnormalized far-field directivity function $\tilde{D}_{ff}^H(\theta,\phi,k)$ characterizes the directivity as

$$\tilde{D}_{ff}^H(\theta,\phi,k) = \sum_{n=0}^{\infty} \sum_{m=-n}^{n} c_n^m(k) k^{-1} i^{n+1} Y_n^m(\theta,\phi), \tag{4}$$

so that the far-field pressure becomes

$$p_{ff}(r,\theta,\phi,k) = \frac{e^{-ikr}}{r} \tilde{D}_{ff}^H(\theta,\phi,k). \tag{5}$$

B. Effect of source translation on far-field directivity

This section derives the relationship between the far-field directivity patterns of a centered and translated source through the KHIT. The KHIT with no volume source terms describes the acoustic pressure within the exterior domain Ω in terms of the pressure $p_s(\mathbf{r}_s)$ and normal particle velocity $u_s(\mathbf{r}_s)$ on the domain boundary S [see Fig. 1(a)],[35]

$$p(\mathbf{r}) = \int\int_S \left[p_s(\mathbf{r}_s) \frac{\partial}{\partial n_s} G(\mathbf{r},\mathbf{r}_s) + i z_0 k u_s(\mathbf{r}_s) G(\mathbf{r},\mathbf{r}_s) \right] dS, \tag{6}$$

where $z_0 = \rho_0 c$ is the characteristic specific acoustic impedance of the fluid, the surface normal $\mathbf{n}_s$ points into Ω, and

$$G(\mathbf{r},\mathbf{r}_s) = \frac{e^{-ik|\mathbf{r}-\mathbf{r}_s|}}{4\pi|\mathbf{r}-\mathbf{r}_s|} \tag{7}$$

is the free-space Green's function. Although Eq. (1) is valid only over Ω_a, the KHIT is valid over the entire acoustic domain Ω.

In the acoustic and geometric far-field, application of the law of cosines and a subsequent binomial approximation allows simplification as $|\mathbf{r}-\mathbf{r}_s| \approx r - \mathbf{r}_s \cdot \hat{\mathbf{r}}$, where $\hat{\mathbf{r}}$ is the unit vector in the directions of $\mathbf{r}$. Substituting this simplified form into the Green's function yields the far-field pressure as[36]

$$p_{ff}(\mathbf{r}) \approx \frac{e^{-ikr}}{4\pi r} \int\int_S \left[p_s(\mathbf{r}_s) \frac{\partial}{\partial n_s} e^{ik\mathbf{r}_s\cdot\hat{\mathbf{r}}} + i z_0 k u_s(\mathbf{r}_s) e^{ik\mathbf{r}_s\cdot\hat{\mathbf{r}}} \right] dS. \tag{8}$$

This result also confirms that the far-field pressure is the product of a spherical wave with a radially independent directivity function, as $\hat{\mathbf{r}}$ only depends on the angular direction. The unnormalized, far-field directivity function produced from the KHIT is then

$$\tilde{D}_{ff}^K(\theta,\phi,k) = \frac{1}{4\pi} \int\int_S \left[p_s(\mathbf{r}_s) \frac{\partial}{\partial n_s} e^{ik\mathbf{r}_s\cdot\hat{\mathbf{r}}} + i z_0 k u_s(\mathbf{r}_s) e^{ik\mathbf{r}_s\cdot\hat{\mathbf{r}}} \right] dS. \tag{9}$$

Two approaches enable the consideration of source translations. The first is to shift the actual source location by $\mathbf{r}''$ and the second is to shift the observation position by $-\mathbf{r}''$. This section contains the derivation for the former, although the derivation to the latter yields an equivalent result.

As suggested by Fig. 1(b), consider a source displacement by $\mathbf{r}''$ so that $\mathbf{r}_s' = \mathbf{r}_s + \mathbf{r}''$. The pressure p' again follows from the KHIT, except with the integration performed over the shifted boundary S'. With the new geometric far-field condition $r \gg R_s + r''$, the far-field approximation becomes $|\mathbf{r}-\mathbf{r}_s'| \approx r - \mathbf{r}_s' \cdot \hat{\mathbf{r}}$. Considering that $\mathbf{r}_s' = \mathbf{r}_s + \mathbf{r}''$, the far-field pressure may be then written as

21 October 2026 17:59:12

$$p'_{ff}(\mathbf{r}) = \frac{e^{-ikr}}{4\pi r} e^{ik\hat{\mathbf{r}}\cdot\mathbf{r}''} \int\int_{S'} \left[p_s(\mathbf{r}'_s) \frac{\partial}{\partial n'_s} e^{ik\mathbf{r}_s\cdot\hat{\mathbf{r}}} + iz_0 k u_s(\mathbf{r}'_s) e^{ik\mathbf{r}_s\cdot\hat{\mathbf{r}}} \right] dS'. \quad (10)$$

The spatial variable $\mathbf{r}'_s$ in Eq. (10) designates the points over the surface S', whereas $\mathbf{r}_s$ in Eq. (8) defines the points over the surface S. Because the pressure and normal particle velocity *distributions*, surface normals, and other properties on these surfaces yield the same values for the same relative positions on S and S' [compare Figs. 1(a) and 1(b)], the integrals in Eq. (10) and Eq. (8) must be equal, such that

$$p'_{ff}(\mathbf{r}) = e^{ik\mathbf{r}''\cdot\hat{\mathbf{r}}} p_{ff}(\mathbf{r}). \quad (11)$$

Using the relationship between the far-field pressure to the far-field directivity patterns expressed in either Eq. (5) or Eq. (8) yields

$$D'_{ff}(\theta, \phi, k) = e^{ik\mathbf{r}''\cdot\hat{\mathbf{r}}} D_{ff}(\theta, \phi, k). \quad (12)$$

The key result of this relationship is that the magnitude of the far-field directivity patterns of translated and untranslated sources are equal,

$$|D'_{ff}(\theta, \phi, k)| = |D_{ff}(\theta, \phi, k)|. \quad (13)$$

This result intuitively follows by considering a measurement array whose radius approaches infinity. Any small shift $r'' \ll r$ becomes negligible when considering the magnitude of the far-field pressure.

Figure 2 illustrates this concept for a theoretical point source distribution comprising 20 sources with equal amplitudes at dodecahedral vertices and a circumradius of $a_d = 0.2$ m centered about the origin. Numerically evaluating the pressure at increasing radii of $a = 1, 2, 10$ m, and in the far-field at 1.5 kHz ($\lambda \approx 0.2$ m) demonstrates how a directional pattern evolves over distance. Figures 2(a)–2(d) show the directivity with the point source distribution centered at the origin, whereas Figs. 2(e)–2(h) show the directivity with the point source distribution translated by $\mathbf{r}'' = (0.7, 0.0, 0.0)$ m, where the x-direction is toward the 0° angle marker.

The translated distribution's directivity pattern at the measurement radius initially appears much different from the untranslated distribution's pattern. However, in the far field, both sources have the same magnitude directivity pattern. Observing the centered directivity pattern's evolution over distance makes some near-field effects apparent, such as deepening interference nulls. Thus, even centered sources require adequate radial distance to overcome near-field effects, highlighting a deficiency in methods that only perform acoustic centering at the array measurement surface. The authors' work in Refs. 33 and 37 includes other results and discussions for a monopole, dipole, and quadrupole. Consequently, although previous works have argued for the need of centering algorithms to correct for directivity pattern perturbations because of source misalignment, Eq. (13)

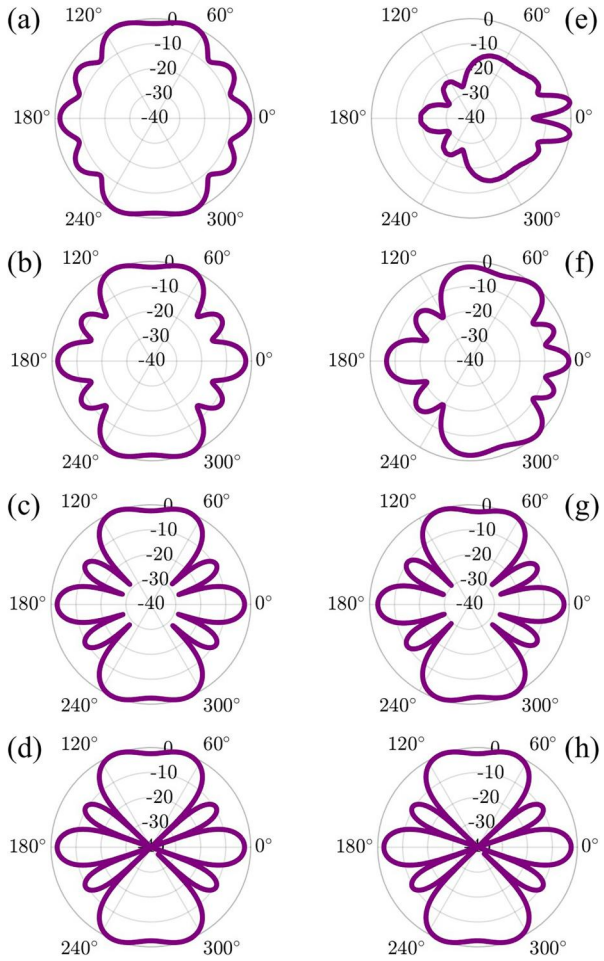


FIG. 2. Directivity patterns of a centered (a)–(d) and translated (e)–(h) 20 point-source dodecahedral distribution at distances (a) and (e) $r = 1$ m, (b) and (f) $r = 2$ m, (c) and (g) $r = 10$ m, and (d) and (h) in the far-field.

demonstrates that far-field propagation *via* acoustical holography is sufficient for obtaining the magnitude far-field pattern.

Although the magnitude far-field patterns of centered and translated sources are equal, a phase shift remains between the original and translated patterns as

$$\angle D'_{ff}(\theta, \phi, k) = k\mathbf{r}'' \cdot \hat{\mathbf{r}} + \angle D_{ff}(\theta, \phi, k), \quad (14)$$

which is associated with the time delay caused by the source translation. Cox[38] arrived at a similar result when he suggested that shifting a simple source by r'' along the z-axis would lead to a phase shift of $kr'' \cos\theta$. Thus, with a knowledge of the far-field directivity magnitude and phase, one may determine the far-field directivity after a source translation by modifying the directivity phase according to Eq. (14).

Another point of consideration arises when a translated source remains relatively close to the geometric array center, such that $r'' \ll a$. If the array is in the acoustic and geometric far field of the centered source so that $a \gg \lambda/2\pi$ and $a \gg R_s$, it remains in the far field of the translated source because it still satisfies the required conditions $a \gg \lambda/2\pi + r''$ and $a \gg R_s + r''$. Thus, the magnitude directivity

21 October 2026 17:59:12

https://doi.org/10.1121/10.0046846

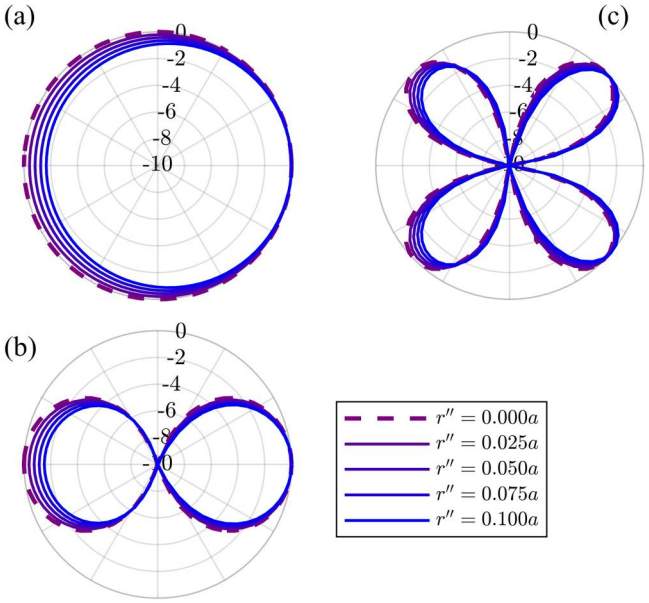


FIG. 3. Changes in directivity patterns because of small translations for a (a) monopole, (b) dipole, and (c) lateral quadrupole. All plots are shown on a 10 dB scale.

patterns of the centered and translated sources will be nearly equivalent.

Figure 3 illustrates this effect by comparing the simulated directivities of a monopole, dipole, and lateral quadrupole with varying displacements no greater than $r'' = 0.1a$ in the x-direction with $ka = 50$. For all sources, even when the displacement reached $0.1a$, the maximum beam pattern error was less than 2 dB. In fact, the significant directivity deviations seen in Fig. 2 resulted from large source displacements relative to the array size. These exaggerated displacements may be unrealistic under normal measurement conditions and can be readily avoided by experimentalists.

Overall, obtaining the commonly desired magnitude far-field directivity pattern requires either (1) a measurement radius satisfying both the acoustic and geometric far-field conditions so that minor variations in source placement becomes negligible or (2) propagating the measured pressure to the far field using acoustical holography. Because the former option is severely limited by measurement chamber size and other practical constraints, the latter option is often the only feasible approach.

However, the ability to perform far-field propagation requires sufficient sampling density to avoid spatial aliasing. Ben Hagai *et al.*[26] showed that for a source band limited to finite expansion degree N, a source displacement r'' increases the number of expansion terms by roughly $\Delta N \approx kr''$. Because the number of sampling positions directly controls the maximum possible expansion degree N,[34] even a minor displacement r'' can lead to a significant increase in sampling requirements at high frequencies. Consequently, although far-field propagation removes the theoretical need for centering algorithms, determining the acoustic center of the source to reduce spatial aliasing effects remains a practical consideration. Reference 37 contains additional discussion and results on the topic of spatial aliasing, including the relationship between commonly used sampling configurations and the maximum allowable translation distance.

C. Acoustic center revisited

The KHIT and general exterior problem do not require an acoustic center to construct the unique solution to the Helmholtz equation. Furthermore, because different approaches to assessing acoustic centers may yield different locations for the same source,[20] the definition, necessity, and benefit of an acoustic center may depend upon the application. For example, when considering the anechoic properties of a test room,[17] one may find the definition of an acoustic center based on $1/r$ decay to be most beneficial. However, for directivity measurements, it seems most beneficial to define the acoustic center as follows:

> The acoustic source center is the origin of the coordinate reference frame from which the observed directional pressure field converges fastest to its magnitude far-field pattern with respect to the observation distance r.

The examples of displaced sources in Fig. 2 and in Ref. 33 help motivate this interpretation. Although the figures show that the centered and translated sources eventually yield the same far-field directivity pattern, the untranslated source patterns converge more rapidly, i.e., with the smallest radial propagation distance.

A converged far-field pattern allows one to safely ignore radial directivity dependence and employ a fixed directivity function dependent only upon the angular coordinates. This simplification has clear advantages in reducing the computational load in wave-based simulations by replacing Eq. (1) with Eq. (5) as well as mitigating near-field effects used in ray-based methods that employ only far-field magnitude patterns.

The proposed definition of the acoustic center reduces to Trott's[18] earlier redefinition for the case of an omnidirectional source at low frequencies. As discussed by Vanderkooy,[22] such a source may be replaced by an equivalent point source located at its acoustic center. Then, the coordinate reference frame from which the observed pressure converges to its omnidirectional far-field pattern with the smallest observation distance r is the frame whose origin is the location of this equivalent point source.

III. ACOUSTIC CENTERING ALGORITHM

Section II demonstrated that far-field propagation is sufficient to obtain the magnitude far-field directivity pattern of a source. However, determining the acoustic center remains beneficial for practical reasons, including minimizing the maximum expansion degree of the source N or optimizing source placement to maximize the spatial-aliasing-limited measurement bandwidth. This section outlines an acoustic centering algorithm to address this need.

Following the acoustic center definition in Sec. II C, assume that there exists a coordinate frame for which the directivity pattern converges fastest over r to the far-field

21 October 2026 17:59:12

result. Then, compared to all other coordinate frames, that coordinate frame should yield the smallest deviation between its directivity evaluated at a fixed radius R and the magnitude far-field directivity pattern. The algorithm's approach is consequently to evaluate the complex-valued pressure field on spheres of radius $R > a$ centered at different candidate positions $\mathbf{r}''$ and compare these near-field results to the extrapolated far-field directivity pattern. The algorithm then selects the acoustic center $\mathbf{r}_c$ as the candidate position, whose corresponding near-field pattern is the closest to the far-field result.

Figure 4 illustrates the concept behind the centering algorithm for three such candidate reference frames for the case of a monopole displaced from the origin. The black circle in Fig. 4(a) represents the measurement sphere in the transverse plane, whereas the solid red dot indicates the location of the displaced monopole. Figure 4(b) shows the monopole's measured directivity on the array surface, with balloon radius and color both indicating level on a relative logarithmic scale. Because of the source placement, the measured directivity pattern differs from the anticipated omnidirectional radiation pattern.

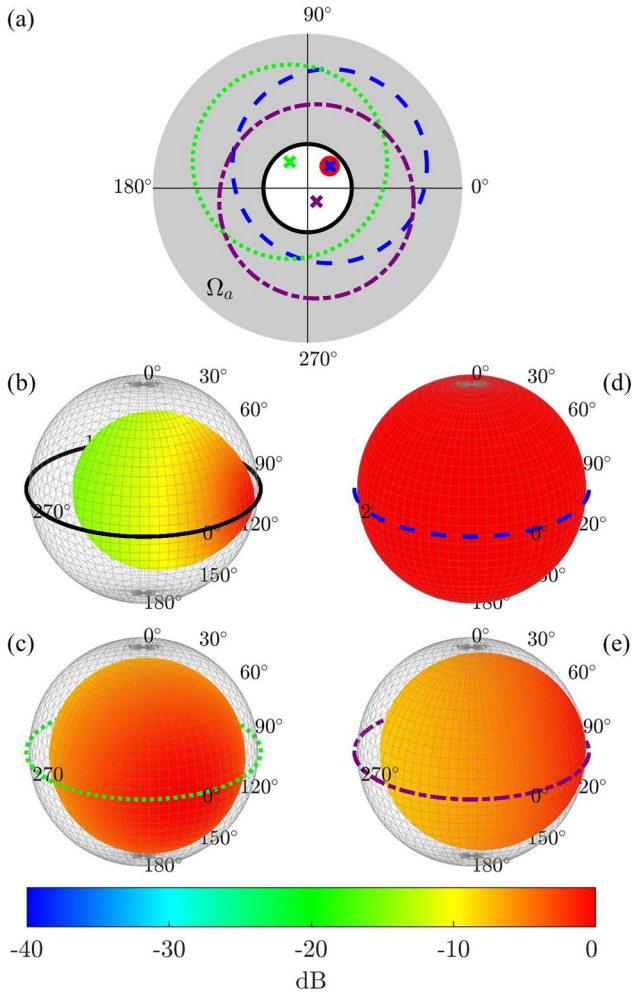


FIG. 4. An illustration motivating the centering algorithm for a monopole source. (a) Diagram of source location (red dot), original sampling sphere (black circle), and extrapolated sampling spheres (green, blue, and purple circles). Directivities evaluated on the (b) original sampling sphere and the extrapolated (c) green-dotted sphere, (d) blue-dashed sphere, and (e) purple dashed-dotted sphere.

After obtaining the far-field magnitude pattern $|D_{ff}(\theta, \phi)|$ by propagating the measured pressure to infinity *via* Eq. (3), the algorithm uses acoustical holography [see Eq. (1)] to calculate the pressure on spheres of radius R centered about candidate positions $\mathbf{r}''$. The coordinates of these spheres are given as

$$\mathbf{r}' = R\hat{\mathbf{r}} + \mathbf{r}'', \tag{15}$$

and three such candidates appear in Fig. 4(a) as green dotted, blue dashed, and purple dashed-dotted circles with $\times$ symbols of the corresponding color indicating their centers $\mathbf{r}''$. Practical computation using acoustical holography requires calculating the candidate sphere's coordinates in Cartesian form using Eq. (15) before transforming them to spherical coordinates to match Eq. (1). Importantly, the sphere radius R must be sufficiently large to ensure that the spherical evaluation surfaces remain in the exterior domain Ω_a $(r > a)$, depicted as the gray region in Fig. 4(a), to ensure valid extrapolation of field quantities *via* Eq. (1).

Figures 4(c)–4(e) show the normalized directivity $|D(r', \theta', \phi')|$ evaluated on each of the candidate spheres, with the encircling colored line indicating the corresponding cross section in Fig. 4(a). Only when the candidate sphere's center coincides with the source's acoustic center does its directivity pattern match the true omnidirectional far-field pattern [Fig. 4(d)].

Quantitatively, the objective function to minimize is the spherically weighted mean-squared error between the normalized magnitude far-field pattern D_{ff} and the normalized magnitude near-field patterns D,

$$J(\mathbf{r}''|R) = \int_0^{\pi}\int_0^{2\pi} \left(|D(r', \theta', \phi')| - |D_{ff}(\theta, \phi)|\right)^2 \sin\theta d\theta d\phi. \tag{16}$$

In practice, numerical integration is necessary to evaluate the integral in Eq. (16).

In all, the steps of the algorithm are as follows:

(1) Measure a sound source's pressure at Q discrete positions and obtain the pressure expansion coefficients c_n^m through a least squares inversion or numerical integration [Eq. (2), Ref. 34].
(2) Evaluate the far-field directivity pattern D_{ff} using the expansion coefficients c_n^m [Eq. (4)].
(3) For each candidate position $\mathbf{r}''$, evaluate the near-field directivity D at the positions given by Eq. (15) by applying acoustical holography [Eq. (1)].
(4) Compute the objective function J using D, D_{ff}, and numerical integration.
(5) The acoustic center is the candidate position $\mathbf{r}''$, which minimizes the objective function.

Several practical implementation details merit further discussion. First, the proposed method is independent of

21 October 2026 17:59:12

https://doi.org/10.1121/10.0046846

how the expansion coefficients c_n^m are obtained. In contrast, previous methods required a least squares inversion with the expansion origin placed at each candidate position $\mathbf{r}''$, which can become numerically unstable for positions far from the measurement origin. Although the proposed method can also use coefficients obtained in this manner, it is not restricted to this approach. For example, the present work will use numerical integration instead of a least squares fit.

Second, the expansion coefficients need only be computed once, after which acoustical holography is used to evaluate the pressure field at arbitrary candidate positions. Consequently, the proposed method requires at most a single matrix inversion, rather than one inversion for every candidate position. This not only results in a substantial reduction in computational cost at high frequencies but also avoids the numerical instabilities associated with least squares fits taken far from the origin.

Third, the spherical sampling grid used to evaluate J is largely arbitrary, provided it has sufficient spatial resolution to avoid aliasing. The present work evaluates J on the same sampling grid used during measurement, although less dense grids could be applied at lower frequencies to save on computational cost.

Finally, the centering algorithm requires selecting an evaluation radius R. This radius should be sufficiently large to satisfy Eq. (1) and avoid near-field effects, yet not so large that the differences between the evaluated directivity patterns and the far-field pattern become negligible. Nevertheless, empirical evaluations found using values of R an order of magnitude larger than a provided sufficient differences to accurately identify the acoustic center while still avoiding near-field effects.

IV. RESULTS

A. Theoretical sources

1. Multipoles

A displaced monopole, dipole, longitudinal quadrupole, and lateral quadrupole are each low-order sources with well-defined acoustic centers. The dipole moment and longitudinal quadrupole moment are in the positive $\hat{\boldsymbol{y}}$ direction, whereas the lateral dipole moments lie in the $\hat{\boldsymbol{x}}$ and $\hat{\boldsymbol{y}}$ directions. The simulations place the source's centers at $\mathbf{r}'' = (0.5, 0.5, 0)$ m and use a frequency of 500 Hz ($kr'' \approx 6.4$), measured with an $a = 1$ m array having 5° resolution in the polar and azimuthal angles. The algorithm uses an $N = 20$ expansion calculated using a Chebyshev–Lobatto spherical quadrature scheme.[39]

The objective function minimums for the case of $R = 10a$ (Fig. 5) align with the source location and acoustic source center for all sources. The objective functions appear convex over the entire cross section of the $a = 1$ m measurement sphere, indicated by the solid black curve. However, the objective functions are not necessarily quadratic with respect to the spatial coordinates. For example, the

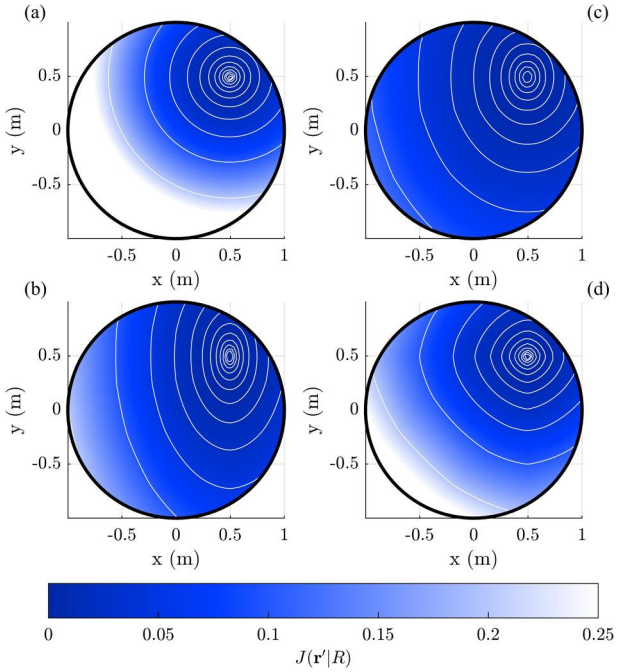


FIG. 5. Contour plots of the objective function at 500 Hz in the x–y plane for a (a) monopole, (b) dipole, (c) longitudinal quadrupole, and (d) lateral quadrupole displaced to position $\mathbf{r}'' = (0.5, 0.5, 0.0)$ m.

monopole shows a spherically symmetric objective function, whereas the dipole and longitudinal quadrupoles have elongated patterns in the directions of the dipole and quadrupole moments. The lateral quadrupole has a rhombus-like pattern. Results using $R = 2a$, $R = 10a$, and $R = 100a$ localized the same acoustic centers to within a relative error of $|\hat{r}_c - r_c|/r_c$ of less than 1% for all cases. However, the $R = 2a$ case had the highest errors, possibly because of near-field effects.

2. Point source distribution

A point source distribution provides a better approximation of a realistic distributed source than multipoles, which are concentrated at a single point. Consider a three-monopole distribution with the sources at $\mathbf{r}_c = (0.5, 0.2, 0.0)$ m, $\mathbf{r}_c = (-0.5, 0.2, 0.0)$ m, and $\mathbf{r}_c = (-0.1, -0.3, 0.0)$ m, and with respective source strengths 2.0 m^3/s, 1.0 m^3/s, and 1.0 m^3/s. At low frequencies, the acoustic center follows as $\mathbf{r}_c = (0.150, 0.075, 0.000)$ m from a center-of-mass formula.[23]

Figure 6 plots several normalized objective function surfaces at 50 Hz ($kr'' = 0.49$) in the x–y plane using the same array and algorithm configuration as for the multipoles. Figure 6(a) plots[28]

$$J_{ss}(\mathbf{r}'') = 1 - \left| \frac{\int_0^{\pi}\int_0^{2\pi} p^2(r', \theta', \phi') \sin\theta d\theta d\phi}{\int_0^{\pi}\int_0^{2\pi} |p(r', \theta', \phi')|^2 \sin\theta d\theta d\phi} \right| \tag{17}$$

an objective function based on the coherent summation of the complex pressure. Figure 6(b) plots[26,28]

21 October 2026 17:59:12

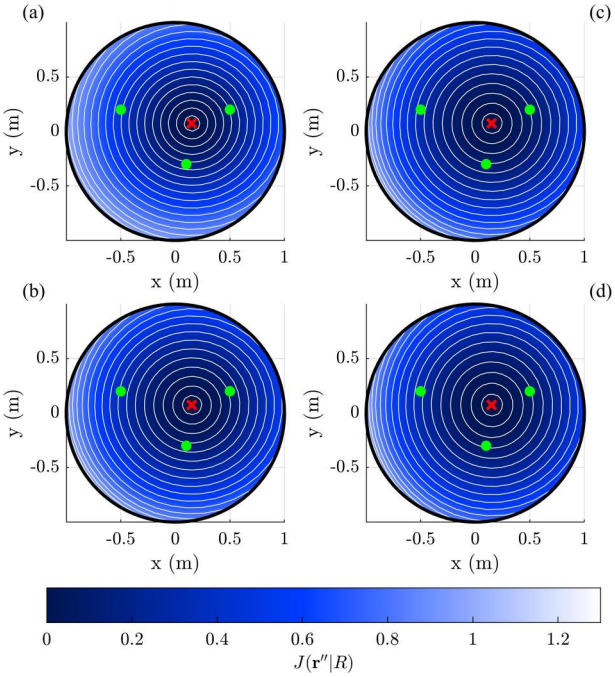


FIG. 6. Objective functions for the acoustic source centering of a three-monopole distribution at 50 Hz. (a) J_{ss}, (b) J_{lo}, (c) J_{ph}, (d) J of the present work.

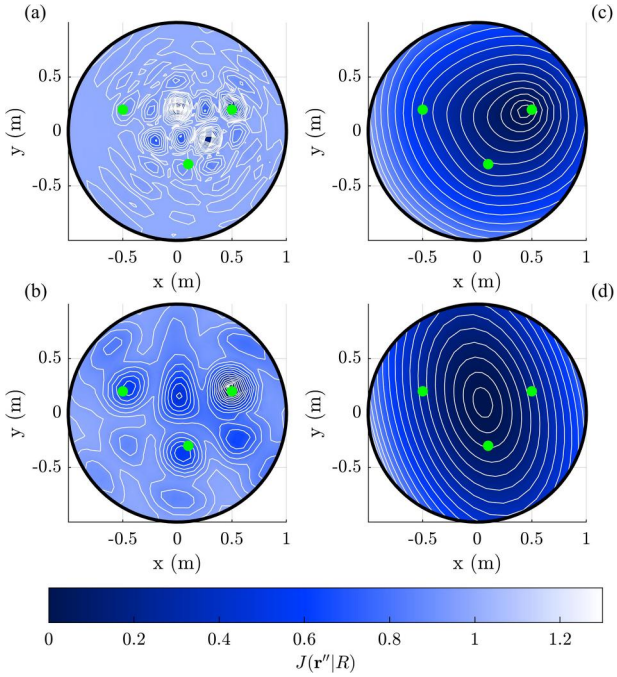


FIG. 7. Objective functions for the acoustic source centering of a three-monopole distribution at 500 Hz. (a) J_{ss}, (b) J_{lo}, (c) J_{ph}, (d) J of the present work.

$$J_{lo}(\mathbf{r}'') = \frac{\sum_{n=0}^{N} n|c_n^{m\prime}|^2}{\sum_{n=0}^{N} |c_n^{m\prime}|^2}, \tag{18}$$

where $c_n^{m\prime}$ are the pressure expansion coefficient calculated in the evaluation coordinate frame with origin $\mathbf{r}''$, an objective function that penalizes energy in higher-degree expansion terms. Figure 6(c) plots[32]

$$J_{ph}(\mathbf{r}'') = -\frac{\sum_{n=0}^{N} |c_n^{0\prime}|^2}{\sum_{n=0}^{N}\sum_{m=-n}^{n} |c_n^{m\prime}|^2}, \tag{19}$$

an objective function based on phase contours in the x–y plane. Finally, Fig. 6(d) plots the proposed objective function J. The three green dots indicate the point source locations, whereas the red $\times$ indicates the theoretical low-frequency acoustic center. The objective functions remain similarly convex in all cases, and their global minima coincide with the low-frequency acoustic center.

Figure 7 presents results for the same numerical experiment but at 500 Hz ($kr'' = 4.93$). As kr'' is not small, the low-frequency acoustic center does not apply. Because the underlying low-order or coherent phase assumptions break down at this frequency, the previously proposed algorithms struggle to identify a meaningful acoustic center. Numerous local minima appear in both J_{ss} and J_{lo}, similar to results reported in Refs. 28 and 26; some of the most significant local minima occur at the point source locations. Conversely, J_{ph} gives a single minimum; however, it converges to the point source with the largest amplitude. Only the proposed method of the present work identifies a single acoustic center located between the point sources.

3. Point source on a sphere

This section compares centering results for the acoustic center of a point source on a rigid sphere of radius a, a higher-order source requiring roughly $N \approx ka$ expansion terms. Jacobsen *et al.*[20] derived theoretical results for this source to show that its acoustic center varies depending on the calculation method.

Figure 8 plots the acoustic center over frequency along the axis from the sphere's center, through the point source, and beyond. The blue dashed line indicates the position $r = a$ of the point source, which is the acoustic center in the absence of the rigid sphere. The green dashed-dotted line indicates the low-frequency acoustic center.[23] The solid black curve shows a theoretical center based on matching $1/r$ decay with an equivalent monopole,[20]

$$r_c(R) = R - \frac{z_0 k Q_{eq}}{4\pi|p(R)|}, \tag{20}$$

where Q_{eq} is the equivalent monopole source strength [see Eq. (18) of Ref. 20 for the derivation of Q_{eq}], and $p(R)$ is the on-axis pressure evaluated at distance R. The red dotted curve indicates the acoustic center determined from this work's proposed technique. For both methods, the formulations

21 October 2026 17:59:12

https://doi.org/10.1121/10.0046846

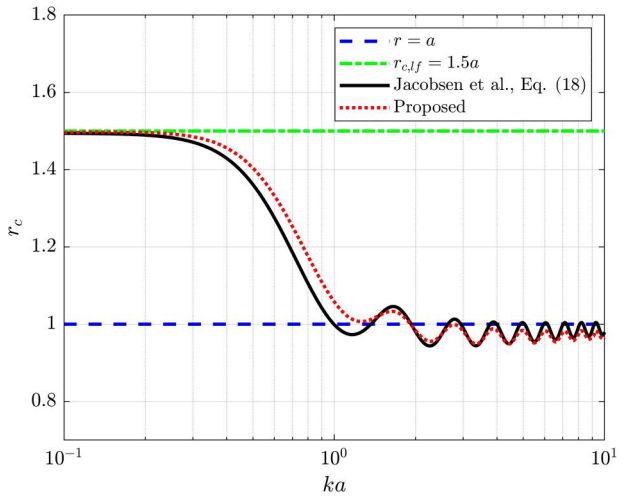


FIG. 8. Frequency-dependent acoustic center results for a point source on a rigid sphere of radius $a = 1$ m.

apply an evaluation distance of $R = 100a$. Because the formulations and definitions of the acoustic center differ, one anticipates some differences between the curves. The $1/r$ acoustic center follows from a single, on-axis observation point, whereas the proposed method uses a global approach that evaluates the source pressure in all directions. Although the curves do not agree perfectly, they have marked similarities. Both converge to the low-frequency acoustic center for $ka \ll 1$. As ka approaches unity, the curves dip toward $r_c = a$. For $ka \geq 1$, the predicted centers undulate about $r_c = a$ then slightly below $r_c = a$.

B. Experimental results

A convex regular polyhedron loudspeaker (RPL) is a real source that exhibits complex radiation patterns above its omnidirectional cutoff frequency.[40] In contrast to a rectangular loudspeaker, it has a clearly defined acoustic center falling at the polyhedron's geometric center, assuming all of its drivers are identical. Measurements of the loudspeaker's directivity employed an $a = 0.97$ m semicircular array consisting of 36 12.7 mm (0.5 in) microphones spaced 5° in the polar angle, with a consequent microphone spacing of about 8.5 cm. Rotating the arc in 5° increments in the azimuthal angle swept out a sampling sphere consistent with the 5° resolution Audio Engineering Society (AES) sampling standard.[41] The expansion coefficients followed from numerical integration using a Chebyshev–Radau quadrature rule accurate up to $N = 34$.[39] This sampling resolution permits measurement of the $R_s = 9.85$ cm source to roughly $k(R_s + r'') \approx 34$ without spatial aliasing effects, e.g., 2.5 kHz when displaced to a position $r'' = 0.6$ m from the origin.[26,29,37]

Because the constructed loudspeaker may have exhibited some asymmetries because of inexact driver matching, nonideal driver behaviors, or imperfect dodecahedron fabrication, complementary simulated dodecahedron directivities clarify whether centering errors resulted from algorithmic limitations or measurement errors and uncertainties. The simulated pressure resulted from a model comprising a rigid sphere of radius $a_l = 9.85$ cm and 12 axially vibrating caps[42,43] with radii $a_d = 2.95$ cm.

Figure 9 shows the 100 Hz results for the measured and simulated loudspeakers displaced to $\mathbf{r}_c = (-0.01, 0.00, -0.58)$ m ($kr_c \approx 1.1$). The extreme displacement in z leads to severe deviations from the anticipated omnidirectional pattern for the measured directivity at the array surface [Fig. 9(a)]. The simulated data [Fig. 9(d)] almost exactly reproduces the effect seen in the measured result, agreeing to within 0.5 dB of the measurement. After far-field propagation [Figs. 9(b) and 9(e)], the directivity converges to the anticipated omnidirectional radiation, with the largest deviation for the measured result remaining within 1.0 dB down from the maximum.

A three-dimensional minimization of J using the Nelder–Mead simplex algorithm on the measured data with $R = 10$ m gave an estimated acoustic center of $\hat{\mathbf{r}}_c = (-0.016, 0.015, -0.60)$ m, yielding a magnitude error of $|\hat{\mathbf{r}}_c - \mathbf{r}_c| = 0.02$ m. The deviations for the simulated data were trivial, suggesting that centering errors for the measured data are likely because of measurement uncertainties or loudspeaker irregularities. Figure 9(c) compares the objective

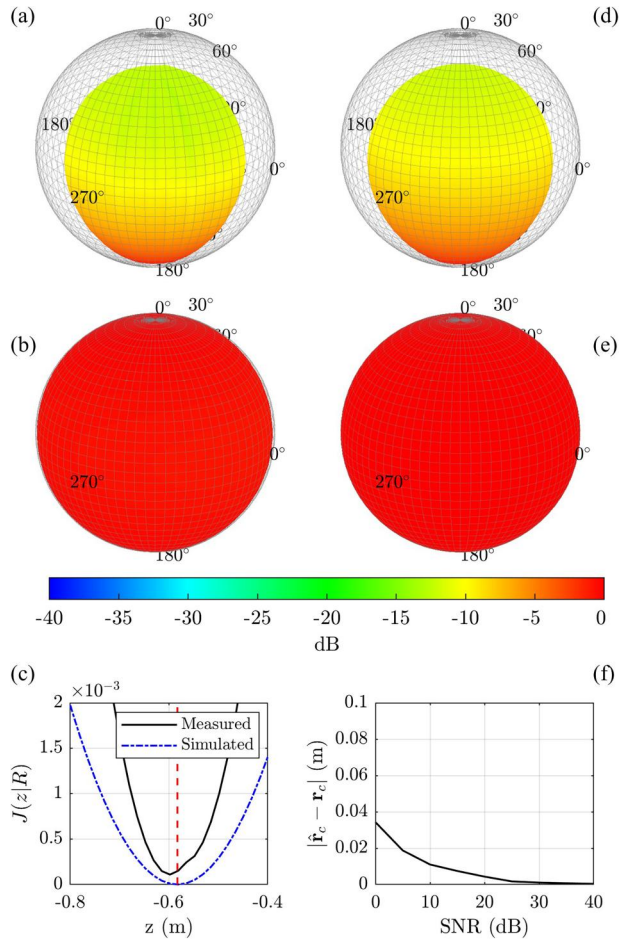


FIG. 9. Acoustic centering of a dodecahedron loudspeaker at 100 Hz using measured (a) and (b) and simulated (d) and (e) data. (a) and (d) Directivity at the array, (b) and (e) far-field propagated directivity, (c) objective function J, (f) simulated localization error for varying SNR.

21 October 2026 17:59:12

functions evaluated along a one-dimensional line parallel to the z-axis and intersecting the known displacement $\mathbf{r}_c$, showing that the simulated data has an overall lower objective function value and is more cleanly aligned about the known acoustic center. The phase relationship given in Eq. (14) permits correcting the far-field phase of the translated source once the acoustic center is known. Applying this adjustment reduced the spherically averaged phase deviation between the simulated translated and centered data from 31° to less than 1°.

Even for at the higher frequency of 3.6 kHz, far-field propagation corrects for deviations seen in the near-field radiation patterns after a $\mathbf{r}_c = (0.0, 0.00, -0.195)$ m ($kr_c \approx 12.9$) displacement in both the measured [Figs. 10(a) and 10(b)] and simulated [Figs. 10(d) and 10(e)] data. The final result is consistent with the complex pattern typical of dodecahedron loudspeakers at higher frequencies.[40] The simulation data agree well with the measured data at the array surface, with deviation errors less than 1.5 dB.

The algorithm localized the acoustic center of the measured data at $\hat{\mathbf{r}}_c = (0.00, 0.00, -0.19)$ m, corresponding to a magnitude deviation of 0.01 m. The centering errors for the simulated data remained trivial. The objective functions evaluated along the z-axis [Fig. 10(c)] show similar trends to the lower frequency case, such as nearly exact centering for the simulated data. Applying the phase correction reduced the spherically averaged phase deviations between the simulated centered and translated data from 122° to only 4°. The higher initial phase deviation resulted from the large kr_c value causing significant phase oscillations in the translated data.

An analysis of noise robustness provides further insight into differences in the algorithm's performance between the measured and simulated data. The analysis repeated the simulated loudspeaker centering experiments but added Gaussian noise to create a signal-to-noise ratio (SNR) ranging from 0 dB to 40 dB, with the upper bound chosen to approximate the measured loudspeaker's SNR of 32 dB and 43 dB for the 100 Hz and 3.6 kHz data, respectively. The magnitude localization error averaged over ten randomized simulations appears in Fig. 9(f) for the 100 Hz case and Fig. 10(f) for the 3.6 kHz case.

For the low frequency case, the localization error remained small. However, by an SNR of 10 dB, the averaged deviation exceeded 0.01 m. The higher frequency case was more sensitive to noise effects, with the magnitude localization error exceeding 0.05 m just below an SNR of 20 dB. The measured data's reported centering accuracy of a few centimeters aligns well with these theoretical predictions, especially considering that the measurements include additional uncertainties such as sensor positioning and non-ideal loudspeaker behavior.

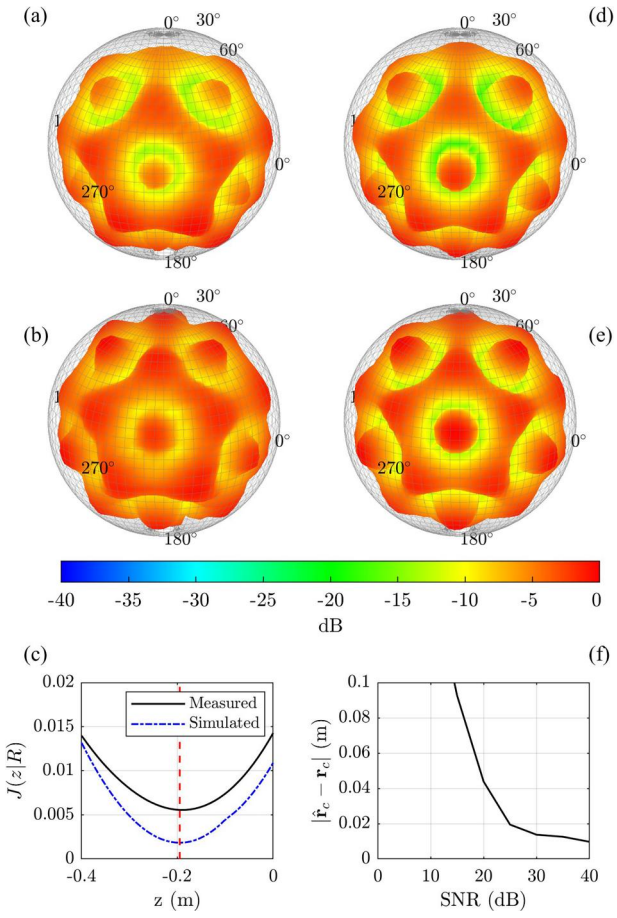


FIG. 10. Acoustic centering of a dodecahedron loudspeaker at 3.6 kHz using measured (a) and (b) and simulated (d) and (e) data. (a) and (d) Directivity at the array, (b) and (e) far-field propagated directivity, (c) objective function J, and (f) simulated localization error for varying SNR.

V. DISCUSSION

Obtaining reliable directivity patterns has been a key motivation for developing source-centering techniques. This work has highlighted several related points. First, a sufficiently large measurement radius and careful attention to the source's location can minimize deviations in magnitude patterns from actual far-field patterns. If one cannot place the array sufficiently far from the source or when the expected acoustic center cannot align with the geometric array center, far-field propagation leads to the centered magnitude far-field pattern. Consequently, for applications where only magnitude values are essential, such as for many implementations of geometrical acoustics,[44] far-field propagation should replace acoustic centering algorithms to overcome the effects of source misalignment.

With the inclusion of directional phase information, several matters require careful consideration. If only the complex far-field pressure is necessary, source translations follow by simply modifying the far-field phase data *via* Eq. (14). For spherical harmonic expansions at variable radii, benefiting some time-domain, wave-based simulations,[45] translation may yield a simplified source representation using fewer expansion coefficients.[26,28] However, it is essential to remember that a change in the coordinate frame origin does not change the unique solution to the Helmholtz equation given by Eq. (1). Both the translated and centered

21 October 2026 17:59:12

directivities and their associated expansions are equally valid, provided that they are properly referenced with respect to their associated coordinate system.

Section IV has demonstrated, the proposed source-centering algorithm succeeds for both large displacements and complex radiation patterns occurring at high frequencies. This characteristic is essential for centering many practical sources, such as loudspeakers or noise-generating sources, that have frequency-dependent acoustic centers or require high-order spherical harmonic expansions. However, adequate spatial sampling is necessary to minimize spatial aliasing because the far-field pressure follows from acoustical holography. This fact implies that the total number and distribution of sampling positions constrain the technique's upper-frequency limit. Consequently, the method may not significantly increase usable bandwidth with low-density sampling schemes compared to other techniques. However, with the higher-density sampling schemes that have been standardized for decades, one can perform acoustic centering at much higher frequencies than previously proposed methods allow.

VI. CONCLUSION

This work has provided perspectives on source translations, acoustic centering, and their effects on measured and far-field directivities. The results demonstrate that far-field magnitude patterns of translated sources are equivalent to those of centered sources, whereas phase shifts compensate for associated time delays. The work has presented an acoustic source-centering algorithm that seeks the reference frame from which the sound pressure field converges with the smallest observation distance to the far-field pattern. Theoretical models and experimental data validated the technique. The algorithm's objective function appears convex at all tested frequencies, and its minimum aligns well with known acoustic centers. However, sampling resolution limits bandwidth because the approach extrapolates the sound pressure to the far field *via* acoustical holography. High-resolution sampling is essential to fully leverage the algorithm's potential and enable acoustic centering at higher frequencies.

Future research could explore alternative approaches to acoustic centering based on far-field phase relationships and develop more robust methods for handling spatial aliasing. It could also determine how to best use frequency-dependent acoustic source centers for source placement during measurements.

ACKNOWLEDGMENTS

The authors gratefully acknowledge funding from the William James and Charlene Fuhriman Strong Family Musical Acoustics Endowed Fellowship.

AUTHOR DECLARATIONS

Conflict of Interest

The authors have no conflicts to disclose.

DATA AVAILABILITY

The data that support the findings of this study are available from the corresponding author upon reasonable request.

[1]F. Otondo and J. H. Rindel, "A new method for the radiation representation of musical instruments in auralizations," Acta Acust. **91**, 902–906 (2005).
[2]J. Meyer, "The sound of the orchestra," J. Audio Eng. Soc. **41**(4), 203–213 (1993).
[3]C.-H. Jeong, J.-G. Ih, C.-H. Yeon, and C.-H. Haan, "Prediction of the acoustic performance of a music hall considering the radiation characteristics of Korean traditional musical sources," J. Acoust. Soc. Kr. **23**(2), 146–161 (2004).
[4]M. Clark, Jr., P. Minter, "Dependence of timbre on the tonal loudness produced by musical instruments," J. Audio Eng. Soc. **12**(1), 28–31 (1964).
[5]S. D. Bellows and T. W. Leishman, "Optimal microphone placement for single-channel sound-power spectrum estimation and reverberation effects," J. Audio Eng. Soc. **71**(1/2), 20–33 (2023).
[6]ANSI S1.1-1994: *American National Standard Acoustical Terminology* (American National Standards Institute, New York, 2004).
[7]L. Beranek and T. Mellow, *Acoustics: Sound Fields, Transducers and Vibration*, 2nd ed. (Academic Press, London, 2019).
[8]H. Dunn and D. W. Farnsworth, "Exploration of pressure field around the human head during speech," J. Acoust. Soc. Am. **10**(3), 184–199 (1939).
[9]P. A. Northrop, "Problems in the analysis of the tone of an open organ pipe," J. Acoust. Soc. Am. **12**(1), 90–94 (1940).
[10]M. S. Ureda, "Apparent apex theory," in *61st Convention of the Audio Engineering Society*, November 3-6, 1978, New York. (AES, 1978), pp. 1–15.
[11]M. S. Ureda, "Apparent apex revisited," in 90th Convention of the Audio Engineering Society, February 19–22, Paris, France. (AES, 1991), pp. 1–22.
[12]M. S. Ureda, "Apparent apex, Part III: The three-dimensional case," https://aes.org/publications/elibrary-page/?id=5550 (Last viewed, 2 October 2026).
[13]M. Vorlander and H. Bietz, "Novel broad-band reciprocity technique for simultaneous free-field and diffuse-field microphone calibration," Acta Acust. **80**, 365–367 (1994).
[14]S. Barrera-Figueroa, K. Rasmussen, and F. Jacobsen, "The acoustic center of laboratory standard microphones," J. Acoust. Soc. Am. **120**(5), 2668–2675 (2006).
[15]G. R. Hruska and W. Koidan, "Free-field method for sound-attenuation measurement," J. Acoust. Soc. Am. **58**(2), 507–509 (1975).
[16]K. A. Cunefare, V. B. Biesel, J. Tran, R. Rye, A. Graf, M. Holdhusen, and A.-M. Albanese, "Anechoic chamber qualification: Traverse method, inverse square law analysis method, and nature of test signal," J. Acoust. Soc. Am. **113**(2), 881–892 (2003).
[17]ISO 3745:2012: *Acoustics–Determination of Sound Power Levels and Sound Energy Levels of Noise Sources Using Sound Pressure—Precision Methods for Anechoic Rooms and Hemianechoic Rooms* (International Organization for Standardization, Geneva, 2012).
[18]W. J. Trott, "Effective acoustic center redefined," J. Acoust. Soc. Am. **62**(2), 468–469 (1977).
[19]IEC 61094-3: *Electroacoustics—Measurement microphones—Part 3: Primary Method for Free-Field Calibration of Laboratory Standard Microphones by the Reciprocity Technique* (International Electrotechnical Commission, Geneva, 2016).
[20]F. Jacobsen, S. B. Figueroa, and K. Rassmussen, "A note on the concept of acoustic center," J. Acoust. Soc. Am. **115**(4), 1468–1473 (2004).
[21]J. Vanderkooy and D. Henwood, "Polar plots for low frequencies: The acoustic centre," in *121st Convention of the Audio Engineering Society, October 5–8, 2006*, San Francisco (AES, 2006), pp. 1–15.
[22]J. Vanderkooy, "The acoustic center: A new concept for loudspeakers at low frequencies," in *120th Convention of the Audio Engineering Society, May 20–23, 2006*, Paris, France (AES, 2006), pp. 1–10.
[23]S. D. Bellows and T. W. Leishman, "On the low-frequency acoustic center," J. Acoust. Soc. Am. **153**(6), 3404–3418 (2023).
[24]S. D. Bellows, "Analytic expressions for the low-frequency acoustic center of dipole radiators," in *Proceedings of the 11th Convention of the*

21 October 2026 17:59:12

European Acoustics Association Forum Acusticum/EuroNoise 2025, EAA, Malaga, Spain (June 23–26, 2025), pp. 4481–4488.
[25]E. G. Williams, *Fourier Acoustics: Sound Radiation and Nearfield Acoustical Holography* (Academic Press, London, 1999).
[26]I. Ben Hagai, M. Pollow, M. Vorländer, and B. Rafaely, "Acoustic centering of sources measured by surrounding spherical microphone arrays," J. Acoust. Soc. Am. **130**(4), 2003–2015 (2011).
[27]J. Hargreaves, "Extending the low frequency acoustic centre concept to directional loudspeakers," https://salford-repository.worktribe.com/preview/2381301/ja_hargreaves_extending_the_low_frequency_acoustic_centre_concept_to_directional_loudspeakers.pdf. (Last viewed, 2 October 2026).
[28]D. Deboy, "Acoustic centering and rotational tracking in surrounding spherical microphone arrays," Master's thesis, Institute of Electronic Music and Acoustics, University of Music and Performing Arts, Graz, Austria, 2010.
[29]S. D. Bellows, J. E. Avila, and T. W. Leishman, "Deriving played trumpet directivity patterns from a multiple-capture transfer-function technique," Acta Acust. **9**, 13 (2025).
[30]D. Deboy and F. Zotter, "Tangential intensity algorithm for acoustic centering," in *Proceedings of the 37th German Annual Conference on Acoustics (DAGA 2011),* Düsseldorf, Germany, 21–24 March 2011 (2011), pp. 321–322.
[31]M. Pollow, G. Behler, and M. Vorländer, "Post-processing and center adjustment of measured directivity data of musical instruments," in *Proceedings Acoustics 2012, IOA*, Nantes, France (April 23–27, 2012), pp. 767–771.
[32]N. R. Shabtai and M. Vorländer, "Acoustic centering of sources with higher-order radiation patterns," J. Acoust. Soc. Am. **137**(4), 1947–1961 (2015).
[33]S. D. Bellows and T. W. Leishman, "Acoustic source centering of musical instrument directivities using acoustical holography," Proc. Mtgs. Acoust. **42**(1), 055002 (2020).
[34]B. Rafaely, *Fundamentals of Spherical Array Processing* (Springer-Verlag, Berlin, 2015), Vol. 8.
[35]A. D. Pierce, *Acoustics: An Introduction to Its Physical Principles and Applications* (Springer, Cham, Switzerland, 2019).
[36]D. Colton and R. Kress, *Inverse Acoustic and Electromagnetic Scattering Theory* (Springer, New York, 2013), 3rd edition.
[37]S. D. Bellows, "Acoustic directivity: Advances in acoustic center localization, measurement optimization, directional modeling, and sound power spectral estimation," Ph.D. dissertation, Brigham Young University, Provo, Utah, 2023.
[38]J. J. R. Cox, "Physical limitations on free-field microphone calibration," Ph.D. thesis, Massachusetts Institute of Technology, Cambridge, MA, 1954.
[39]S. D. Bellows and T. W. Leishman, "Application of Chebyshev quadrature rules to equiangular spherical and hemispherical directivity measurements," J. Audio Eng. Soc. **72**(1/2), 44–58 (2024).
[40]T. W. Leishman, S. Rollins, and H. M. Smith, "An experimental evaluation of regular polyhedron loudspeakers as omnidirectional sources of sound," J. Acoust. Soc. Am. **120**(3), 1411–1422 (2006).
[41]AES56-2008: *AES Standard on Acoustics—Sound Source Modeling—Loudspeaker Polar Radiation Measurements* (Audio Engineering Society, New York, 2019).
[42]E. Skudrzyk, *The Foundations of Acoustics* (Springer-Verlag, New York, 1971).
[43]J. Mortensen, "Computing the directivities of platonic-solid loudspeakers," Senior thesis, Brigham Young University, Provo, Utah, 2014.
[44]L. Savioja and U. P. Svensson, "Overview of geometrical room acoustic modeling techniques," J. Acoust. Soc. Am. **138**(2), 708–730 (2015).
[45]S. Bilbao, J. Ahrens, and B. Hamilton, "Incorporating source directivity in wave-based virtual acoustics: Time-domain models and fitting to measured data," J. Acoust. Soc. Am. **146**(4), 2692–2703 (2019).

21 October 2026 17:59:12